Journal of Magnetic Resonance 194 (2008) 89–98

Contents lists available at ScienceDirect

Journal of Magnetic Resonance

journal homepage: www.elsevier.com/locate/jmr

Clean HMBC: Suppression of strong-coupling induced artifacts in HMBC spectra

Peter Würtz [a], Perttu Permi [a], Niels Chr. Nielsen [b], Ole W. Sørensen [c,*]

[a] *Program in Structural Biology and Biophysics, Institute of Biotechnology, University of Helsinki, FI-00014 Helsinki, Finland*
[b] *Center for Insoluble Protein Structures (inSPIN), Interdisciplinary Nanoscience Center (iNANO) and Department of Chemistry, University of Aarhus, DK-8000 Aarhus C, Denmark*
[c] *Department of Chemistry, Technical University of Denmark, Kemitorvet 207, DK-2800 Kgs. Lyngby, Denmark*

ARTICLE INFO

Article history:
Received 19 April 2008
Revised 4 June 2008
Available online 7 June 2008

Keywords:
HMBC
H2BC
Low-pass *J* filter
Strong coupling
Small molecule NMR

ABSTRACT

A new experiment, *clean* HMBC, is introduced for suppression of strong-coupling induced artifacts in HMBC spectra. The culprits of these artifacts are an inherent shortcoming of low-pass *J* filters in the presence of strong coupling and the ^{1}H π pulse in the middle of the evolution period aimed at suppressing evolution under heteronuclear *J* couplings and ^{1}H chemical shifts. A π pulse causes coherence transfer in strongly coupled spin systems and, as is well known in e.g., homonuclear *J* spectra, this leads to peaks that would not be there in the absence of strong coupling. Similar artifacts occur in HMBC spectra, but they have apparently been overlooked, presumably because they have been assigned to inefficiency of low-pass *J* filters or not noticed because of a coarse digital resolution in the spectra. *Clean* HMBC is the HMBC technique of choice for molecules notorious for strong coupling among protons, such as carbohydrates, and the new technique is demonstrated on D-mannose. Finally, a fundamental difference between HMBC and H2BC explains why strong-coupling artifacts are much less of a problem in the latter type of spectra.

1. Introduction

Long range ^{13}C–^{1}H correlation spectra are indispensable in NMR studies of small molecules. For example, the HMBC experiment [1] provides a valuable map of *n*-bond correlations ($n \geqslant 2$) based on non-vanishing $^nJ_{CH}$ coupling constants. The experiment typically exhibits good sensitivity for three-bond correlations, while it is less reliable for two-bond correlations because some of the $^2J_{CH}$ coupling constants are vanishingly small. For protonated carbons, this shortcoming is overcome by the H2BC experiment [2,3] that relies on $^1J_{CH}$ and $^3J_{HH}$ couplings for magnetization transfer and yields almost exclusively a map of two-bond ^{1}H–^{13}C correlations. The HMBC and H2BC experiments are complementary and both are recommended as part of a standard protocol for structure elucidation of small molecules.

Although progress has been made toward uniform excitation over a range of $^nJ_{CH}$ coupling constants in HMBC [4,5] such spectra usually exhibit very large differences in peak intensities, not only because of varying coherence transfer efficiency but also because of large variations in width of ^{1}H multiplets due to homonuclear couplings. Hence artifact suppression is extremely important in HMBC spectra, as key peaks can be of very low intensity. Whilst pulsed-field gradients take care of the major artifacts such as dominating magnetization from molecules without ^{13}C isotopes, one-bond correlations must be eliminated by further spin manipulations.

Low-pass *J* filters (LPJF) [6] have been designed to suppress unwanted one-bond correlations that would otherwise obscure multiple-bond correlations in heteronuclear long-range correlation spectra. In principle, any degree of suppression can be achieved by applying higher-order filters, but it has been observed that whilst the expected degree of suppression is observed for weakly coupled spin systems that is not the case for strong coupling. Indeed, even perfectly tuned delays in the LPJFs or going to higher-order filters have little effect on the intensity of one-bond artifacts in HMBC spectra in the presence of strong coupling. Interestingly, H2BC spectra do not suffer from this problem even when the very same LPJFs are applied.

This paper explains these phenomena and introduces a modified HMBC experiment, *clean* HMBC, where good suppression of undesired one-bond correlation peaks is achieved even in case of strong coupling. The phenomena are first explained in simple terms before presenting a more rigorous theoretical analysis. In the limit of weak coupling, HMBC and *clean* HMBC spectra are identical.

2. The origin of strong-coupling artifacts in heteronuclear long-range correlation spectra

For the purpose of explaining the origin of the strong-coupling artifacts it suffices to consider an ABX spin system where X is the

* Corresponding author. Fax: +45 4588 3136.
E-mail address: ows@kemi.dtu.dk (O.W. Sørensen).

1090-7807/$ - see front matter © 2008 Elsevier Inc. All rights reserved.
doi:10.1016/j.jmr.2008.06.002

^{13}C spin and A and B are protons with A one-bond coupled to X. Although the spin states of A and B are mixed in the eigenfunctions of the spin system, the eigenfunctions can be characterized as being predominantly A or predominantly B. Inspired by the notation of Thrippleton et al. [7], we refer to predominantly A and predominantly B as {A} and {B}, respectively. This provides a useful picture when the two spins are not extremely strongly coupled.

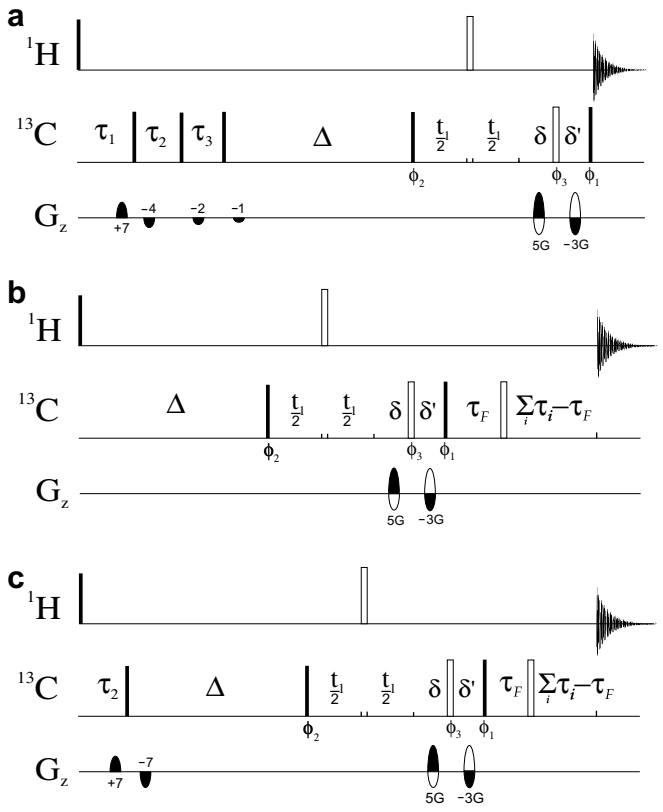

Fig. 1. (a) HMBC pulse sequence with initial 3rd order low-pass *J* filter. (b) HMBC with terminal LPJF in MBOB manner [4]. (c) *Clean* HMBC with both an initial and a terminal LPJF for suppression of strong-coupling induced one-bond correlations. Narrow and wide bars represent π/2 and π pulses, respectively, of phase *x* unless otherwise indicated. The gradients of the LPJF can be set an order of magnitude weaker than the gradients used for the formation of heteronuclear gradient echoes. The delays for the 3rd order LPJF are $\tau_1 = 1/2\ [{}^1J_{min} + 0.07({}^1J_{max} - {}^1J_{min})]^{-1}$, $\tau_2 = ({}^1J_{max} + {}^1J_{min})^{-1}$, $\tau_3 = 1/2\ [{}^1J_{max} - 0.07({}^1J_{max} - {}^1J_{min})]^{-1}$, δ is the gradient delay and $\sum_i \tau_i$ is the sum of pertinent LPJF delays. The terminal filter settings are $\tau_F^{1st} = \{0, \tau_2\}$, $\tau_F^{2nd} = \{0, \tau_1, \tau_3, \tau_1 + \tau_3\}$ and $\tau_F^{3rd} = \{0, \tau_1, \tau_2, \tau_3, \tau_1 + \tau_2, \tau_1 + \tau_3, \tau_2 + \tau_3, \tau_1 + \tau_2 + \tau_3\}$ for 1st, 2nd and 3rd order filter, respectively. The recommended phase cycle is an even number of steps out of $\phi_1 = \{x, -x, -x, x\}$, $\phi_2 = \{x, x, 4(-x), x, x\}$, $\phi_3 = \{4(x), 4(y), 4(-x), 4(-y)\}$ with the receiver phase alternating between *x* and *–x*. For molecules with a large ^{13}C chemical shift range, it is recommended to apply off-resonance compensated composite pulses such as $90_x180_y90_x$ or adiabatic inversion pulses for the π(C) pulses in these pulse sequences. The pulse sequence code for *clean* HMBC for Varian spectrometers is available at www.biocenter.helsinki.fi/bi/NMR.

In the conventional HMBC pulse sequence of Fig. 1a, the initial π/2(H) pulse excites transverse {A} and {B} magnetization that then passes through a low-pass *J* filter. For weak coupling, this filter suppresses A magnetization whilst B magnetization is affected only to a small extent. However, in case of strong coupling, {A} is not entirely "one-bond-coupled" and {B} is not entirely "long-range-coupled", which can be seen as the origin of the shortcoming of LPJFs applied to strongly coupled spin systems. As a further complication in HMBC, the combined action of the π/2(C) pulses and the π(H) pulse in the middle of the t_1 evolution period acting on {B} involved in heteronuclear two-spin coherence with X converts some of {B} into {A}. Likewise, {A} magnetization leaking through the LPJF and involved in heteronuclear two-spin coherence with X gets partly converted to {B} coherence. These coherence transfer pathways and their spectral implications will be discussed in more detail below.

For example, {A} magnetization initially eliminated by the LPJF is recreated after the evolution period leading to a peak split by the one-bond coupling constant in the acquisition dimension no matter how effective the initial LPJF might be. This explains why strong coupling is much less of a problem in H2BC than in HMBC, as the key difference between HMBC and H2BC in the context of strong coupling is that the LPJF in H2BC, in contrast to HMBC, is at the end of the pulse sequence.

Hence a possible remedy for strong-coupling artifacts in HMBC spectra could be to place the LPJF at the end of the pulse sequence. However, due to the antiphase character of the desired magnetization, a conventional LPJF [6] would not work, as it would suppress the entire HMBC spectrum. Fortunately, a nondestructive LPJF [4] can be applied to accomplish the necessary low-pass *J* filtering at the end of the HMBC sequence in order to suppress strong-coupling induced artifacts. Nevertheless, as indicated above and discussed in more detail below, it is worthwhile to maintain an LPJF in the beginning of the sequence. Hence HMBC and *clean* HMBC differ in the way low-pass *J* filtering is performed.

3. The strongly coupled three-spin system consisting of two protons and a ^{13}C spin

The eigenfunctions and eigenfrequencies of a general ABX spin system are compiled in Table 1 that also contains the corresponding items for the weakly coupled AMX spin system for comparison [8].

In the absence of manipulations to the X spin, it is convenient to split the AB part of the Hamiltonian for an ABX spin system into two independent AB Hamiltonians corresponding to the X spin being in either the α or the β state:

Table 1
AMX and ABX eigenfunctions and eigenfrequencies[a]

ABX eigenfunctions	ABX eigenfrequencies	AMX eigenfunctions	AMX frequencies
1. $\|\alpha\alpha\boldsymbol{\alpha}\rangle$	$1/2[\omega_A + \omega_B + \omega_X + \pi(J_{AB} + J_{AX} + J_{BX})]$	1. $\|\alpha\alpha\boldsymbol{\alpha}\rangle$	$1/2[\omega_A + \omega_B + \omega_X + \pi(J_{AB} + J_{AX} + J_{BX})]$
2. $\|\alpha\alpha\boldsymbol{\beta}\rangle$	$1/2[\omega_A + \omega_B - \omega_X + \pi(J_{AB} - J_{AX} - J_{BX})]$	2. $\|\alpha\alpha\boldsymbol{\beta}\rangle$	$1/2[\omega_A + \omega_B - \omega_X + \pi(J_{AB} - J_{AX} - J_{BX})]$
3. $\cos\theta_\alpha\|\alpha\beta\boldsymbol{\alpha}\rangle + (-)\sin\theta_\alpha\|\beta\alpha\boldsymbol{\alpha}\rangle$	$1/2[\omega_X - \pi J_{AB}] + (-)\Lambda_\alpha$	3. $\|\alpha\beta\boldsymbol{\alpha}\rangle$	$1/2[\omega_A - \omega_B + \omega_X + \pi(-J_{AB} + J_{AX} - J_{BX})]$
4. $\cos\theta_\alpha\|\beta\alpha\boldsymbol{\alpha}\rangle - (+)\sin\theta_\alpha\|\alpha\beta\boldsymbol{\alpha}\rangle$	$1/2[\omega_X - \pi J_{AB}] - (+)\Lambda_\alpha$	4. $\|\beta\alpha\boldsymbol{\alpha}\rangle$	$1/2[-\omega_A + \omega_B + \omega_X + \pi(-J_{AB} + J_{AX} - J_{BX})]$
5. $\cos\theta_\beta\|\alpha\beta\boldsymbol{\beta}\rangle + (-)\sin\theta_\beta\|\beta\alpha\boldsymbol{\beta}\rangle$	$1/2[-\omega_X - \pi J_{AB}] + (-)\Lambda_\beta$	5. $\|\alpha\beta\boldsymbol{\beta}\rangle$	$1/2[\omega_A - \omega_B - \omega_X + \pi(-J_{AB} - J_{AX} + J_{BX})]$
6. $\cos\theta_\beta\|\beta\alpha\boldsymbol{\beta}\rangle - (+)\sin\theta_\beta\|\alpha\beta\boldsymbol{\beta}\rangle$	$1/2[-\omega_X - \pi J_{AB}] - (+)\Lambda_\beta$	6. $\|\beta\alpha\boldsymbol{\beta}\rangle$	$1/2[-\omega_A + \omega_B - \omega_X + \pi(-J_{AB} + J_{AX} - J_{BX})]$
7. $\|\beta\beta\boldsymbol{\alpha}\rangle$	$1/2[-\omega_A - \omega_B + \omega_X + \pi(J_{AB} - J_{AX} - J_{BX})]$	7. $\|\beta\beta\boldsymbol{\alpha}\rangle$	$1/2[-\omega_A - \omega_B + \omega_X + \pi(J_{AB} - J_{AX} - J_{BX})]$
8. $\|\beta\beta\boldsymbol{\beta}\rangle$	$1/2[-\omega_A - \omega_B - \omega_X + \pi(J_{AB} + J_{AX} + J_{BX})]$	8. $\|\beta\beta\boldsymbol{\beta}\rangle$	$1/2[-\omega_A - \omega_B - \omega_X + \pi(J_{AB} + J_{AX} + J_{BX})]$

[a] $\sin 2\theta_{\alpha/\beta} = \pi J_{AB}/\Lambda_{\alpha/\beta}$, $\cos 2\theta_{\alpha/\beta} = \{(\omega_A - \omega_B)/2 \pm \pi(J_{AX} - J_{BX})/2\}/\Lambda_{\alpha/\beta}$ where $\Lambda_{\alpha/\beta} = \sqrt{\left(\frac{\omega_A - \omega_B}{2} \pm \pi\frac{J_{AX} - J_{BX}}{2}\right)^2 + (\pi J_{AB})^2}$. For $(\omega_A - \omega_B)/2 \pm \pi(J_{AX} - J_{BX})/2 < 0$ the sign of $\cos 2\theta_{\alpha/\beta}$ is reversed and signs indicated in parentheses apply.

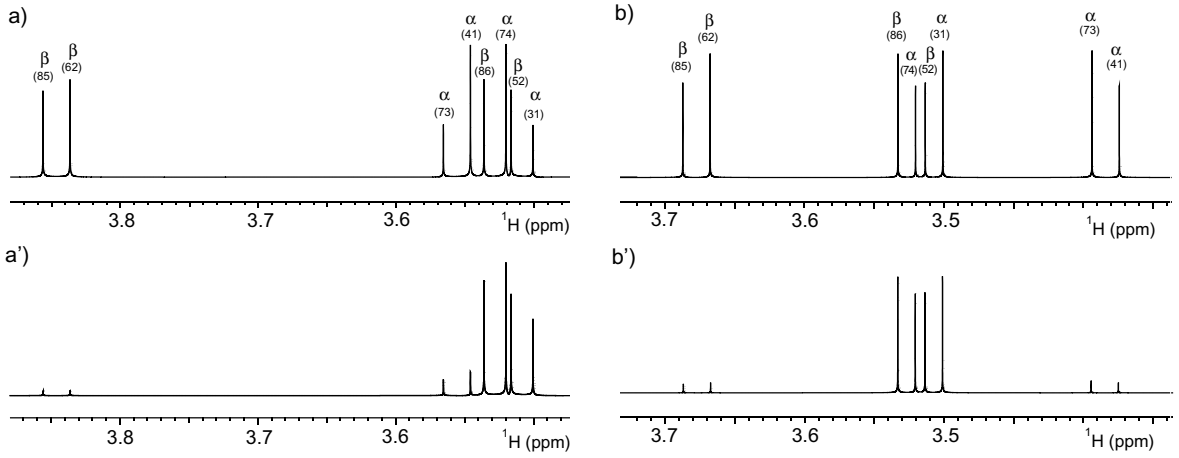

Fig. 2. Simulated spectra of ABX spin systems using SIMPSON [13] for a B_0 field corresponding to a Larmor frequency of 500 MHz: (a) and (b) $\pi/2$(H) – acq.; (a′) and (b′) $\pi/2$(H) – τ–$\pi/2$(C) – acq. with $\tau = (2J_{AX})^{-1}$. The spectra are shown in absolute-value mode and the resonance numbering refers to the single-quantum coherences listed in Table 2. (a) and (a′) The spin system is the $H_5^A - H_4^B - C_5^X$ subset in α-D-mannose with the parameters $\nu_A - \nu_B = -90$ Hz, $J_{AB} = 9.8$ Hz, $J_{AX} = 146$ Hz and $J_{BX} = 7.0$ Hz. The strong coupling parameters are $\sin(2\theta_\alpha) = 0.43$, and $\sin(2\theta_\beta) = 0.061$ and the intensities of the lines are given in Table 2. (b) and (b′) Spin system parameters as above except $\nu_A - \nu_B = -7$ Hz, and thus $\sin(2\theta_\alpha) = 0.078$, and $\sin(2\theta_\beta) = 0.064$.

$$H_{AB(\alpha)} = (\omega_A + \pi J_{AX})A_z + (\omega_B + \pi J_{BX})B_z + 2\pi J_{AB}(A_zB_z + A_xB_x + A_yB_y) \quad (1a)$$

$$H_{AB(\beta)} = (\omega_A - \pi J_{AX})A_z + (\omega_B - \pi J_{BX})B_z + 2\pi J_{AB}(A_zB_z + A_xB_x + A_yB_y). \quad (1b)$$

The extent of mixing the A and B spin functions in the ABX eigenfunctions within the X^α and X^β subsystems is conveniently described in terms of the strong-coupling parameter $\theta_{\alpha/\beta}$ defined as

$$\tan(2\theta_{\alpha/\beta}) = 2\pi J_{AB}/(\omega_A - \omega_B \pm \pi(J_{AX} - J_{BX})) \quad (2)$$

where α/β indicates the state of spin X. The spin system approaches weak coupling when $\theta_{\alpha/\beta} \to 0$, i.e., when the difference in A and B chemical shifts dominates the one-bond coupling constant. Otherwise, typically only one of the two subsystems will exhibit significant strong coupling, e.g., the X^α part when $\omega_A - \omega_B$ and $J_{AX} - J_{BX}$ are about equal but of opposite signs. This is illustrated in Fig. 2a with the AB part of an ABX spectrum: the X^β part is essentially a weakly coupled doublet of a doublet whilst the X^α part has the "roof" pattern characteristic of a strongly coupled two-spin system. Clearly, when the chemical shift difference between the A and B spins is about equal to half the one-bond coupling constant, one of the two subsystems is very strongly coupled whilst the other is essentially weakly coupled.

Fig. 2b illustrates the case of $\omega_A \approx \omega_B$ that would indicate extremely strong coupling in the absence of $^1J_{CH}$ but with this coupling constant included the spin system is relatively weakly coupled.

4. Low-pass *J* filtering in the strongly coupled ABX system

For weak coupling, the four A-spin lines in Fig. 2a (i.e., 85, 62, 73, and 41) would all have the same intensity and upon a free precession delay of $\tau = (2J_{AX})^{-1}$ there would be a π phase difference between the (85) and (73) resonances and likewise between (62) and (41). A $\pi/2$(C) pulse applied to this antiphase state transfers the entire A-spin magnetization into heteronuclear two-spin coherence and this is the mechanism of low-pass *J* filtering whilst the B-spin system will only experience a minor loss, as $J_{BX} \ll J_{AX}$.

Turning to strong coupling there are several factors that are indicative of possible imperfection of the LPJF in case of strong coupling: (i) the four pertinent intensities are no longer equal, (ii) the resonances are no longer purely A or purely B, and (iii) the eigenfrequencies are no longer just linear combinations of a chemical shift and the *J*s, and (iv) the $\pi/2$(C) pulse of the LPJF causes coherence transfer between {A} and {B}.

For illustration, Fig. 2a′ shows in absolute-value mode the spectrum of the same spin system as in Fig. 2a after a first-order LPJF $\pi/2$(H) – τ – $\pi/2$(C) – acq., with $\tau = (2J_{AX})^{-1}$. It is seen that reasonable suppression is obtained for {A}X^β (85 and 62) whilst suppression is much less effective for {A}X^α (73 and 41) that is part of the strongly coupled X^α subsystem. Note also the significant intensity redistribution within the {B} multiplet that virtually is unaffected by the LPJF in case of weak coupling.

Fig. 2b′ shows the result of applying the same LPJF to the spin system in Fig. 2b. The residual {A} signals are as expected all of about equal intensity and intermediate between the two extremes of Fig. 2a′. The two examples in Fig. 2a′ and b′ support the general conclusion that the more strongly coupled the subspin system is the less effective is the low-pass *J* filter and the more prone to artifacts becomes HMBC-type spectra.

The result of a density matrix calculation on an ABX spin system subjected to the LPJF $\pi/2$(H) – τ – $\pi/2$(C) – acq., with $\tau = (2J_{AX})^{-1}$ is compiled in Table 2. The table contains both the exact intensity expressions and their Taylor expansions to first order in θ_α and θ_β. These expansions represent reasonable approximations for many spin systems and can be simplified further by inserting parameters for special cases of interest. For example, the phase factors e_{ij} can be approximated based on the applicable $\omega_A - \omega_B$ and on J_{AX} dominating J_{BX} and J_{AB}.

Fig. 3 shows simulated exact intensity curves as functions of τ in the LPJF for the two-spin systems of Fig. 2. The simulations show that an LPJF delay of $\tau = (2J_{AX})^{-1} = 3.42$ ms still is the best compromise for the strongly coupled ABX spin system. For the spin system in Fig. 2a and a′ the suppression of the {A}X^β resonances 85 and 62 is similar to the case of weak coupling (though one common minimum at $\tau = (2J_{AX})^{-1}$ in case of weak coupling) whilst the intensity curves for the {A}X^α resonances 73 and 41 are rather flat and clearly illustrate the imperfection of LPJF in the presence of strong coupling. For the spin system in Fig. 2b and b′ all four intensity curves for the {A} resonances are similar and correspond to suppression to about 10% for $\tau = (2J_{AX})^{-1}$.

Fig. 3 further shows considerable intensity redistribution within the {B} multiplet for both spin systems, something that does not pose any complication for application to HMBC.

Table 2
Amplitudes of the eight AB resonances of an ABX spin system after a 1st order LPJF

	Standard 1D	Amplitude after LPJF	Amplitude to 1st order in θ_α and θ_β
{85} = $\{A^-B^\beta X^{(\beta}\}$	$1/4\,(1-\sin(2\theta_\beta))$	$1/4\,\lvert -s_\alpha c_\alpha c_\beta e_{74} + s_\alpha c_\alpha c_\beta e_{73} + c_\beta^2 c_\beta e_{74} - c_\alpha^2 c_\beta e_{73} - s_\alpha s_\beta c_\alpha e_{73} + s_\alpha s_\beta c_\alpha e_{74} + s_\beta c_\alpha^2 e_{73} - s_\beta c_\alpha^2 e_{74} - s_\beta c_\beta^2 e_{73} + c_\beta c_\beta e_{85} - s_\beta e_{85}\rvert$	$1/4\,\lvert e_{73} + e_{85} - \theta_\beta e_{74} + \theta_\alpha e_{73} - \theta_\beta e_{74} - \theta_\beta e_{85}\rvert$
{62} = $\{A^-B^\alpha X^{(\beta}\}$	$1/4\,(1+\sin(2\theta_\beta))$	$1/4\,\lvert s_\alpha s_\beta c_\alpha e_{41} - s_\alpha s_\beta c_\alpha e_{31} + s_\beta c_\alpha^2 e_{31} + s_\beta c_\alpha^2 e_{41} - c_\beta c_\beta e_{62} - s_\beta c_\alpha c_\beta e_{31} + s_\alpha c_\alpha c_\beta e_{41} + c_\alpha^2 c_\beta e_{31} - c_\beta^2 c_\beta e_{41} - c_\beta e_{31}\rvert$	$1/4\,\lvert e_{41} + e_{62} - \theta_\alpha e_{41} + \theta_\beta e_{31} + \theta_\beta e_{62} + \theta_\beta e_{31}\rvert$
{73} = $\{A^-B^\beta X^{(\alpha}\}$	$1/4\,(1-\sin(2\theta_\alpha))$	$1/4\,\lvert s_\beta c_\alpha c_\beta e_{86} - s_\beta c_\alpha c_\beta e_{85} + c_\alpha c_\beta^2 e_{86} + c_\alpha e_{73} + s_\alpha e_{73} - s_\alpha s_\beta c_\beta e_{86} - s_\alpha s_\beta c_\beta e_{85} + s_\alpha c_\beta^2 e_{86} + s_\alpha e_{85}\rvert$	$1/4\,\lvert e_{73} + e_{85} + \theta_\alpha e_{73} + \theta_\alpha e_{86} + \theta_\beta e_{86} - \theta_\beta e_{85}\rvert$
{41} = $\{A^-B^\alpha X^{(\alpha}\}$	$1/4\,(1+\sin(2\theta_\alpha))$	$1/4\,\lvert c_\alpha e_{41} - s_\alpha e_{41} - s_\alpha s_\beta c_\beta e_{62} + s_\alpha c_\beta^2 e_{52} - s_\alpha e_{62} - s_\alpha c_\beta^2 e_{52} + s_\beta c_\alpha c_\beta e_{62} - c_\alpha c_\beta^2 e_{62} + c_\alpha e_{52}\rvert$	$1/4\,\lvert e_{41} + e_{62} - \theta_\alpha e_{41} - \theta_\beta e_{52} + \theta_\beta e_{62} - \theta_\beta e_{52}\rvert$
{86} = $\{A^\beta B^-X^{(\beta}\}$	$1/4\,(1+\sin(2\theta_\beta))$	$1/4\,\lvert s_\beta s_\beta c_\alpha e_{74} - s_\beta s_\beta c_\alpha e_{73} - s_\beta c_\alpha^2 e_{73} + s_\beta c_\beta^2 e_{74} - c_\beta e_{86} - s_\beta e_{86} - s_\alpha c_\alpha c_\beta e_{74} + s_\alpha c_\alpha c_\beta e_{73} + c_\alpha^2 c_\beta e_{74} - c_\beta^2 c_\beta e_{73} - c_\beta e_{73}\rvert$	$1/4\,\lvert e_{86} + e_{74} - \theta_\alpha e_{74} + \theta_\alpha e_{73} + \theta_\beta e_{73} + \theta_\beta e_{86}\rvert$
{74} = $\{A^\beta B^-X^{(\alpha}\}$	$1/4\,(1+\sin(2\theta_\alpha))$	$1/4\,\lvert c_\alpha e_{74} - s_\alpha e_{74} - s_\alpha s_\beta c_\beta e_{86} + s_\alpha s_\beta c_\beta e_{85} - s_\alpha c_\beta^2 e_{86} + s_\beta c_\alpha c_\beta e_{86} - c_\alpha c_\beta^2 e_{85} + c_\alpha c_\beta^2 e_{86} + c_\alpha e_{85}\rvert$	$1/4\,\lvert e_{86} + e_{74} - \theta_\alpha e_{74} - \theta_\alpha e_{85} + \theta_\beta e_{86} - \theta_\beta e_{85}\rvert$
{52} = $\{A^\alpha B^-X^{(\beta}\}$	$1/4\,(1-\sin(2\theta_\beta))$	$1/4\,\lvert -s_\alpha c_\alpha c_\beta e_{41} + s_\alpha c_\alpha c_\beta e_{31} + c_\beta c_\beta e_{41} - c_\alpha^2 c_\beta e_{31} + s_\alpha s_\beta c_\alpha e_{41} + s_\alpha s_\beta c_\alpha e_{31} + s_\beta c_\alpha^2 e_{41} - s_\beta c_\beta^2 e_{31} + c_\beta c_\beta e_{52} - s_\beta e_{52}\rvert$	$1/4\,\lvert e_{31} + e_{52} + \theta_\alpha e_{31} - \theta_\alpha e_{41} - \theta_\beta e_{41} - \theta_\beta e_{52}\rvert$
{31} = $\{A^\alpha B^-X^{(\alpha}\}$	$1/4\,(1-\sin(2\theta_\alpha))$	$1/4\,\lvert s_\beta c_\alpha c_\beta e_{62} - s_\beta c_\alpha c_\beta e_{52} + c_\alpha c_\beta^2 e_{62} - c_\alpha + c_\beta^2 e_{62} + c_\alpha e_{31} + s_\alpha e_{31} - s_\alpha s_\beta c_\beta e_{52} + s_\alpha s_\beta c_\beta e_{62} - s_\alpha c_\beta^2 e_{52} + s_\alpha c_\beta^2 e_{62} + s_\alpha e_{52}\rvert$	$1/4\,\lvert e_{31} + e_{52} + \theta_\alpha e_{31} + \theta_\alpha e_{62} + \theta_\beta e_{62} - \theta_\beta e_{52}\rvert$

$c_{\alpha/\beta} = \cos(\theta_{\alpha/\beta})$, $s_{\alpha/\beta} = \sin(\theta_{\alpha/\beta})$ and $e_{ij} = \exp(i(\omega_j - \omega_i)\tau)$.

5. Additional peaks in HMBC spectra caused by strong coupling

For illustration, a simulation of the conventional HMBC pulse sequence with an initial perfectly tuned 1st order LPJF applied to an ABX spin system in mannose at 500 MHz is shown in Fig. 4a, however, with the strong-coupling term $2\pi J_{AB}(A_zB_z + A_xB_x + A_yB_y)$ of the Hamiltonian replaced by $2\pi J_{AB}A_zB_z$ in order to have the weak-coupling spectrum for reference. The result of the spectrum simulation including the strong-coupling term is shown in Fig. 4b. A comparison between Fig. 4a and b reveals insignificant differences in the {B} multiplet. On the other hand, {A} peaks are absent for the weak-coupling case but several ^1J split multiplets appear at different F_1 frequencies as a result of strong coupling.

Fig. 4c shows the corresponding spectrum resulting from applying a perfectly tuned 1st order LPJF at the end of the HMBC sequence instead of in the beginning. While this represents a considerable improvement over the conventional spectrum in Fig. 4b, particularly efficient suppression of the least strongly coupled $\{A\}X^\beta$ part of the spectrum, other strong-coupling artifacts show up for the strongly coupled $\{A\}X^\alpha$ and {B} part at different F_1 frequencies.

As the artifact patterns are different in Fig. 4b and c the natural next step is to apply a LPJF both in the beginning and at the end of the pulse sequence. The result shown in Fig. 4d confirms expectations, as most of the strong-coupling artifacts are suppressed. The only significant remaining strong-coupling artifact is in the $\{A\}X^\beta$ subsystem close to the {B} resonances, as was also the case for the spectrum after LPJF in Fig. 2b. Depending on the digital resolution in the HMBC spectrum this subsystem may or may not be resolved in practice.

Finally, Fig. 4e and f show the corresponding H2BC spectrum without and with, respectively, the strong-coupling term in the Hamiltonian. As is evident, the H2BC spectrum is virtually free of strong-coupling artifacts.

The appearance of signals in F_1 at frequencies that are not the ^{13}C chemical shift modulated by J_{HH} is a result of strong coupling inducing proton–proton coherence transfer by the π(H) pulse. In the case of HMBC with an initial LPJF (Fig. 4b) the artifacts are due to coherence transfer from {B} to {A} and are suppressed by applying an LPJF prior to acquisition. In the same manner, artifacts present in HMBC with a terminal LPJF (Fig. 4c) arise due to coherence transfer from {A} to {B} and these are suppressed by an LPJF in the beginning of the sequence as in conventional HMBC. Hence in the case of strongly coupled spin systems it is important to have LPJFs both in the beginning and at end of the sequence to obtain the cleanest spectra.

It is well known that a π pulse causes coherence transfer between strongly coupled spins A and B [9,10]. This holds also for double-quantum and zero-quantum ABX coherences as long as the strong coupling is between an active and the passive spin, e.g., $A^\alpha B^+X^+$. In the ABX spin system there are of relevance prior to π(H) four double-quantum and four zero-quantum coherences involving the X spin, of which four is with {B} and the other four with {A}:

$$\begin{aligned}
\{B\}: \{A^\alpha B^+X^+\} &= \{15\}, \quad \{A^\beta B^+X^+\} = \{48\},\\
\{A^\alpha B^+X^-\} &= \{23\}, \quad \{A^\beta B^+X^-\} = \{67\},\\
\{A\}: \{A^+B^\alpha X^+\} &= \{16\}, \quad \{A^+B^\beta X^+\} = \{38\},\\
\{A^+B^\alpha X^-\} &= \{24\}, \quad \{A^+B^\beta X^-\} = \{57\}.
\end{aligned}$$

In Table 3 are listed the possible coherence transfers by the π(A,B) pulse in the middle of the t_1 period along with the associated amplitudes and the resulting effective modulation frequencies in ω_1. An example of a coherence transfer caused by the π(H) pulse is

$$\{A^\beta B^+X^+\} \overset{\pi(A_x+B_x)}{\rightarrow} \cos 2\theta_\alpha \{A^\alpha B^-X^+\} - \sin 2\theta_\alpha \{A^-B^\alpha X^+\}. \tag{3}$$

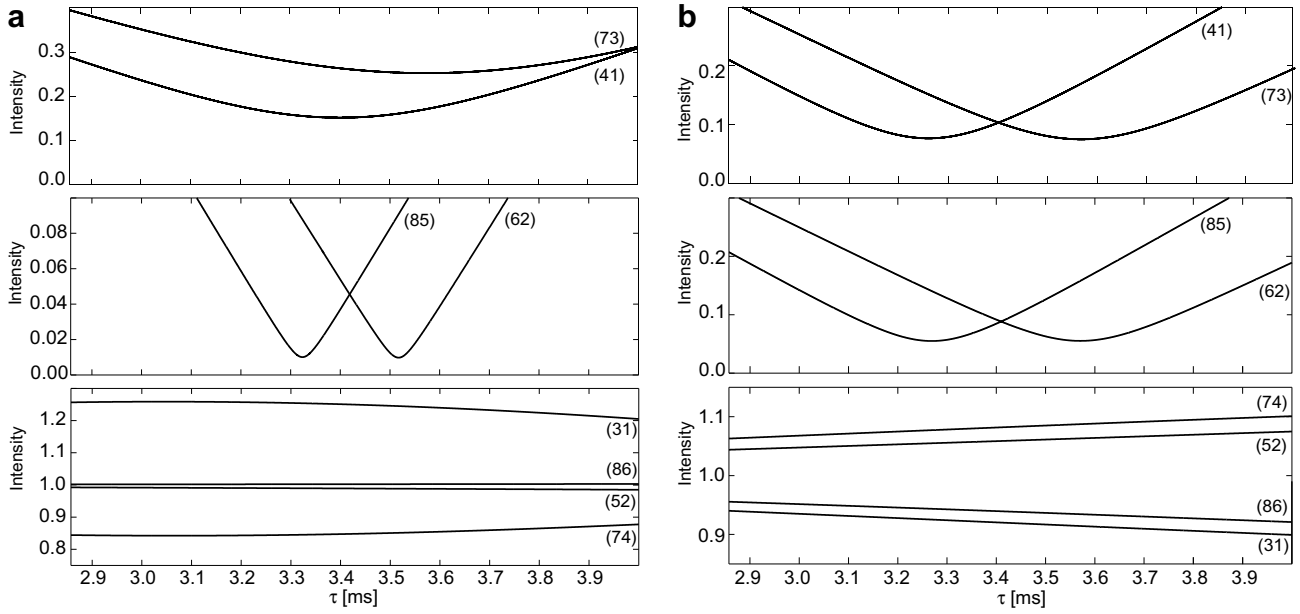

Fig. 3. Resonance intensities after LPJF as functions of the τ delay for (a) the spin system in Fig. 2a and a′, and (b) the spin system in Fig. 2b and b′. The intensities are normalized with respect to the respective resonance intensities without LPJF as shown in Fig. 2a and b.

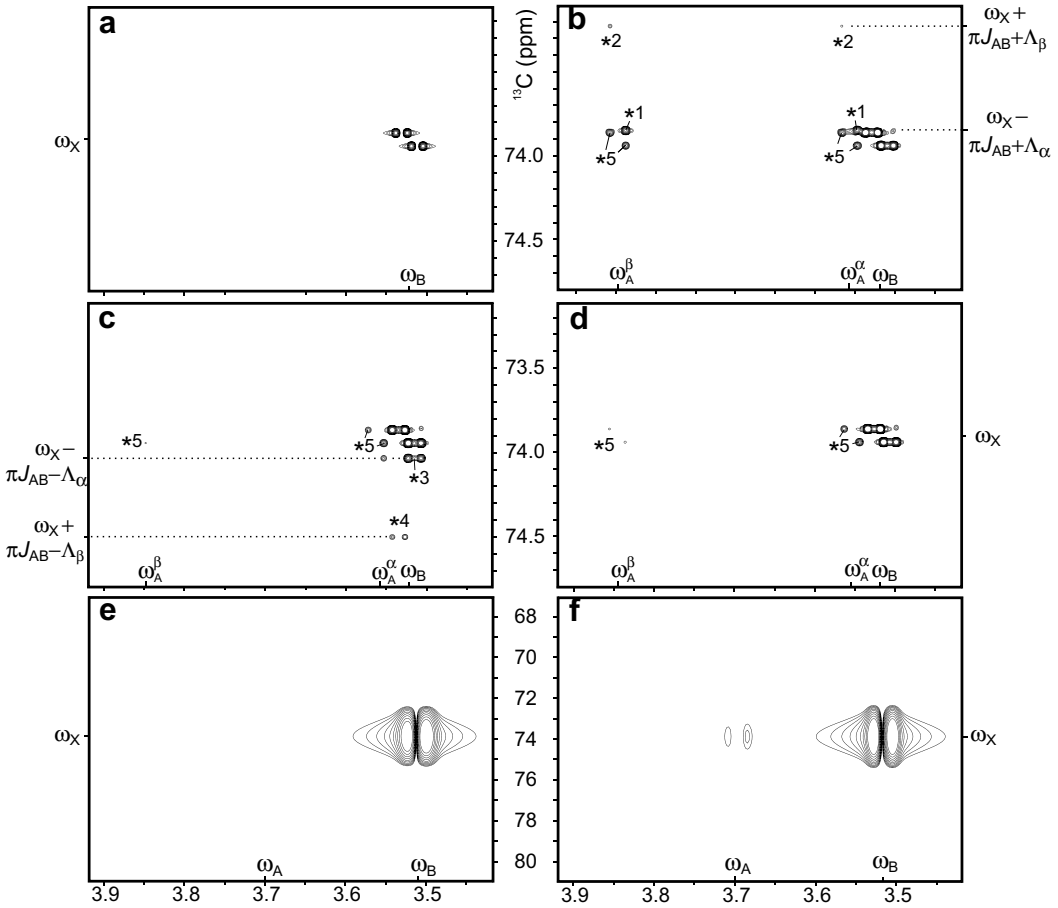

Fig. 4. Simulations of 2D spectra for the same spin system as in Fig. 2a involving 1st order LPJFs exactly tuned to $^1J_{AX}$. (a) Weak-coupling HMBC with initial LPJF, i.e., with the strong coupling term of the Hamiltonian replaced by the corresponding weak-coupling one. (b) HMBC with initial LPJF. (c) HMBC with terminal LPJF. (d) *clean* HMBC, i.e., HMBC with both an initial and a terminal LPJF. (e) Weak-coupling H2BC. (f) H2BC. The spectra are simulated with SIMPSON [13] and processed with NMRpipe [14]. The spin system parameters are as in Fig. 2a and the strong coupling shifts are Λ_α = 11 Hz, Λ_β = 80 Hz. HMBC long-range transfer delay was set to Δ = 65 ms. 512 points were sampled for a spectral width of 1000 Hz in both dimensions and apodized with squared sinebell functions. Only the echo parts of the HMBC spectra are shown. The H2BC spectra were simulated with sequence settings as in Nyberg et al. [2] with 96 t_1 increments on a spectral width of 10 kHz, apodized with squared sinebell functions and phased to pure absorption. The numbered asterisks mark strong coupling artifacts referred to in the text and in Table 3.

Table 3
Coherence transfer amplitudes and resulting t_1 frequency modulations in HMBC of an ABX spin system

Echo	$\{32\}^{-+} = \{A^zB^-X^+\}$	$\{76\}^{-+} = \{A^\beta B^-X^+\}$	$\{42\}^{-+} = \{A^-B^zX^+\}$	$\{75\}^{-+} = \{A^-B^\beta X^+\}$
$\{15\}^{++} =$		$\cos(2\theta_\beta)$		*2: + (−) $\sin(2\theta_\beta)$
$\{A^zB^+X^+\}$		$-[\omega_X + \pi J_{AB}]$		$-[\omega_X + \pi J_{AB} - (+)\,\Lambda_\beta]$
$\{48\}^{++} =$	$\cos(2\theta_\alpha)$		*1: −(+) $\sin(2\theta_\alpha)$	
$\{A^\beta B^+X^+\}$	$-[\omega_X - \pi J_{AB}]$		$-[\omega_X - \pi J_{AB} - (+)\Lambda_\alpha]$	
$\{16\}^{++} =$		*4: −(+) $\sin(2\theta_\beta)$		$\cos(2\theta_\beta)$
$\{A^+B^zX^+\}$		$-[\omega_X + \pi J_{AB} + (-)\Lambda_\beta]$		$-[\omega_X + \pi J_{AB}]$
$\{38\}^{++} =$	*3: + (−)$\sin(2\theta_\alpha)$		$\cos(2\theta_\alpha)$	
$\{A^+B^\beta X^+\}$	$-[\omega_X - \pi J_{AB} + (-)\Lambda_\alpha]$		$-[\omega_X - \pi J_{AB}]$	
Antiecho	$\{A^zB^-X^-\} = \{51\}^{--}$	$\{A^\beta B^-X^-\} = \{84\}^{--}$	$\{A^-B^zX^-\} = \{61\}^{--}$	$\{A^-B^\beta X^-\} = \{83\}^{--}$
$\{23\}^{+-} =$		$\cos(2\theta_\alpha)$		+ (−)$\sin(2\theta_\alpha)$
$\{A^zB^+X^-\}$		$\omega_X - \pi J_{AB}$		$\omega_X - \pi J_{AB} + (-)\Lambda_\alpha$
$\{67\}^{+-} =$	$\cos(2\theta_\beta)$		−(+) $\sin(2\theta_\beta)$	
$\{A^\beta B^+X^-\}$	$\omega_X + \pi J_{AB}$		$\omega_X + \pi J_{AB} + (-)\Lambda_\beta$	
$\{24\}^{+-} =$		−(+) $\sin(2\theta_\alpha)$		$\cos(2\theta_\alpha)$
$\{A^+B^zX^-\}$		$\omega_X - \pi J_{AB} - (+)\Lambda_\alpha$		$\omega_X - \pi J_{AB}$
$\{57\}^{+-} =$	+(−)$\sin(2\theta_\beta)$		$\cos(2\theta_\beta)$	
$\{A^+B^\beta X^-\}$	$\omega_X + \pi J_{AB} - (+)\Lambda_\beta$		$\omega_X + \pi J_{AB}$	

For example, coherence $\{A^zB^+X^+\} = \{15\}^{++}$ is transferred to coherence $\{A^\beta B^-X^+\} = \{76\}^{-+}$ with an amplitude $\cos(2\theta_\beta)$ and the resulting t_1 modulation frequency is $-(\omega_X + \pi J_{AB})$. Signs in parentheses indicate the results for $(\omega_A - \omega_B)/2 \pm \pi(J_{AX} - J_{BX})/2 < 0$. The upper half is the echo part and the lower half the antiecho part. The numbered asterisks refer to the different artifact types in Fig. 4.

This particular coherence transfer is the origin of artifact number *1 in Fig. 4b. The frequency modulations can be derived from Table 1 by using the evolution of the density matrix σ_{ij} according to

$$\sigma_{ij} \xrightarrow{Ht} \sigma_{ij} \exp(i(\omega_j - \omega_i)t), \tag{4}$$

where H is the free precession Hamiltonian and ω_i and ω_j are eigenfrequencies.

The intensities and frequency modulations in Table 3 are in agreement with the results obtained from the numerical simulations in Fig. 4. The four echo-part coherence transfers give rise to the artifact types marked 1–4 in Fig. 4b and c. The π(H)-induced artifact intensity is according to Eq. (4) proportional to $\sin(2\theta_{\alpha/\beta})$. In the simulated case (Fig. 4b) the intensity of the strongest π(H)-induced artifact is about 45% of the main peak intensity, which is in quantitative agreement with the spin-system parameters.

Notably, LPJF leakage arising from non-suppressed {A} magnetization in the initial LPJF is mixed during the evolution period and gives rise to symmetric signals at X^α and X^β of the A spin (artifact number *5 in Fig. 4b), whereas the leakage is asymmetric when a terminal LPJF is incorporated (artifact number *5 in Fig. 4c and d).

The modulation frequencies in the indirect dimension ($\omega_X \pm \Lambda_{\alpha/\beta} \pm \pi J_{AB}$) are reminiscent of homonuclear J spectra [7] if the X frequency modulation is disregarded. However, owing to the numerous passive homonuclear couplings and the low digital resolution used experimentally on the ^{13}C axis, the smallest frequency shift of Λ_α and Λ_β (and thus the most intense artifact) is normally not resolved in HMBC spectra. For this reason the artifacts are not necessarily observable experimentally for the case with only a terminal LPJF (Fig. 4c), while the artifacts arising from only initial LPJF (Fig. 4b) are clearly visible as one-bond coupled signals occurring at frequencies where a one-bond coupled signal would also otherwise occur, e.g., from inefficient low-pass J filtering. Hence, the combined result of LPJF leakage, due to strong coupling or mistuning, and the π(H) artifacts combine to the overall intensity of the one-bond correlated signals. Fig. 4d illustrates the general feature that the *clean* HMBC experiment provides good suppression of strong-coupling artifacts, both those due to the initial LPJF and the π(H) pulse, if they are not too close to the genuine signals of the long-range coupled proton. Such peaks are, however, typically not resolved with the resolution of HMBC-type spectra.

Strongly coupled spin systems also occur without one-bond couplings, e.g., involving quaternary carbons $^{13}C_X$–^{12}C–$^1H_A{}^1H_B$. These spin systems do not, however, cause significant spectral artifacts. The strong-coupling induced coherence transfer from {A} to {B} results in signals that merge with the signals from the desired long-range coherence transfer pathways for the usual resolution in HMBC spectra.

6. Implementation of the *clean* HMBC experiment

As has been made evident in the preceding description and illustrations, suppression of strong-coupling induced artifacts in HMBC spectra is conveniently done by low-pass J filtering both in the beginning and at the end of the pulse sequence. There are many ways of combining the two LPJFs as to what order to use and whether they should be independent or not. We have chosen to apply an overall 3rd order LPJF as is commonly used in HMBC experiments. In this filter, shown in Fig. 1c, there are three delays, τ_1, τ_2, and τ_3, tuned according to ^1J [4,5], and $\tau_2 = (^1J_{max} + {}^1J_{min})^{-1}$ is effected in the beginning of the sequence whilst the two other steps are placed at the end. In other words, the most effective low-pass J filtering is at the end of the sequence, which reflects the fact that this is required for suppression of the most severe strong-coupling induced artifacts. Weakly coupled spin systems are invariant to where the LPJF is placed in the pulse sequence and hence the response to *clean* HMBC from such spin systems is the same as if the 3rd order LPJF were placed in the beginning of the pulse sequence as in conventional HMBC (Fig. 1a).

The desired magnetization at the end of the HMBC pulse sequence is antiphase with respect to heteronuclear long-range coupling constants, and therefore it is necessary to apply a non-destructive LPJF. This can be implemented in a manner analogously to the MBOB pulse sequence for simultaneous recording of HMBC and coupled HSQC-type spectra [4]. The procedure is outlined in Fig. 1b and c and works as follows: a series of transients with different delays τ_F are acquired and coadded [4,5]. For the overall 3rd order LPJF with two of the steps at the end, as applied in this work, this results in a $2 \times 2 = 4$ step LPJF cycle. The step in the beginning of the sequence is as usual performed with gradients and hence does not increase the minimum number of scans. *Clean* HMBC data are processed in exactly the same way as conventional HMBC data. *Clean* MBOB extending *clean* HMBC to MBOB [4,5] would apply a non-destructive LPJF both in the beginning and at the end of the pulse sequence.

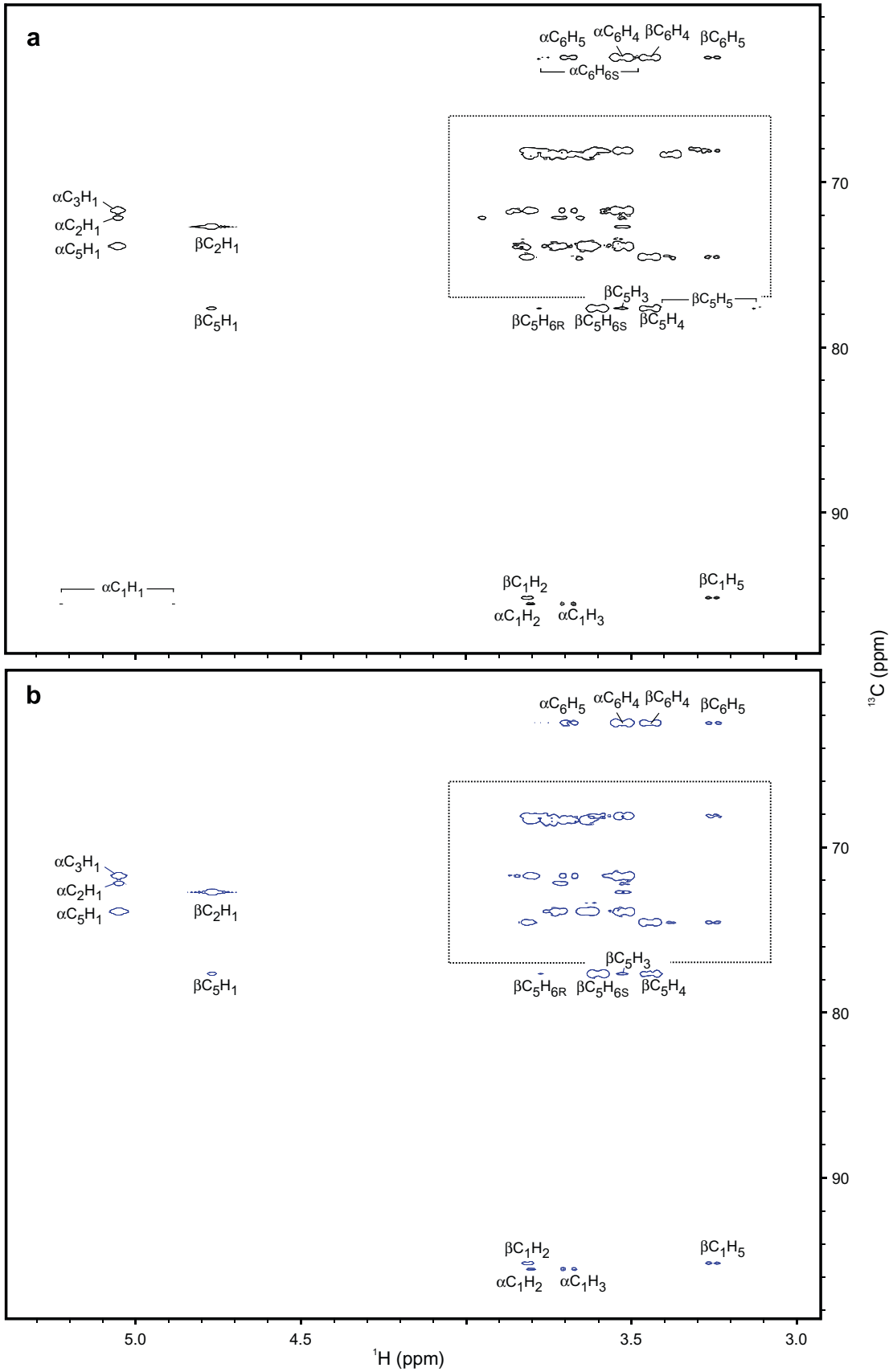

Fig. 5. HMBC spectra of 40 mM D-mannose in D_2O acquired on a Varian Unity Inova 500 MHz spectrometer. (a) Conventional HMBC and (b) *clean* HMBC. The spectra were recorded with 16 transients per FID and 256 t_1 increments. The number of complex points in the acquisition dimension was 1024 and the acquisition time 170.7 ms for all the experiments. The relaxation delay was 1 s, $^nJ_{CH}$ transfer delay Δ = 65 ms, and the range for the overall 3rd order low-pass J filter delay settings was 140 Hz < $^1J_{CH}$ < 175 Hz. The data matrices covering 6 and 3 kHz in F_1 and F_2, respectively, were subjected to linear prediction in t_1 doubling the number of points and apodized using squared cosinebell in t_1 and a $\pi/4$-shifted squared sinebell in t_2 prior to 2D Fourier transformation.

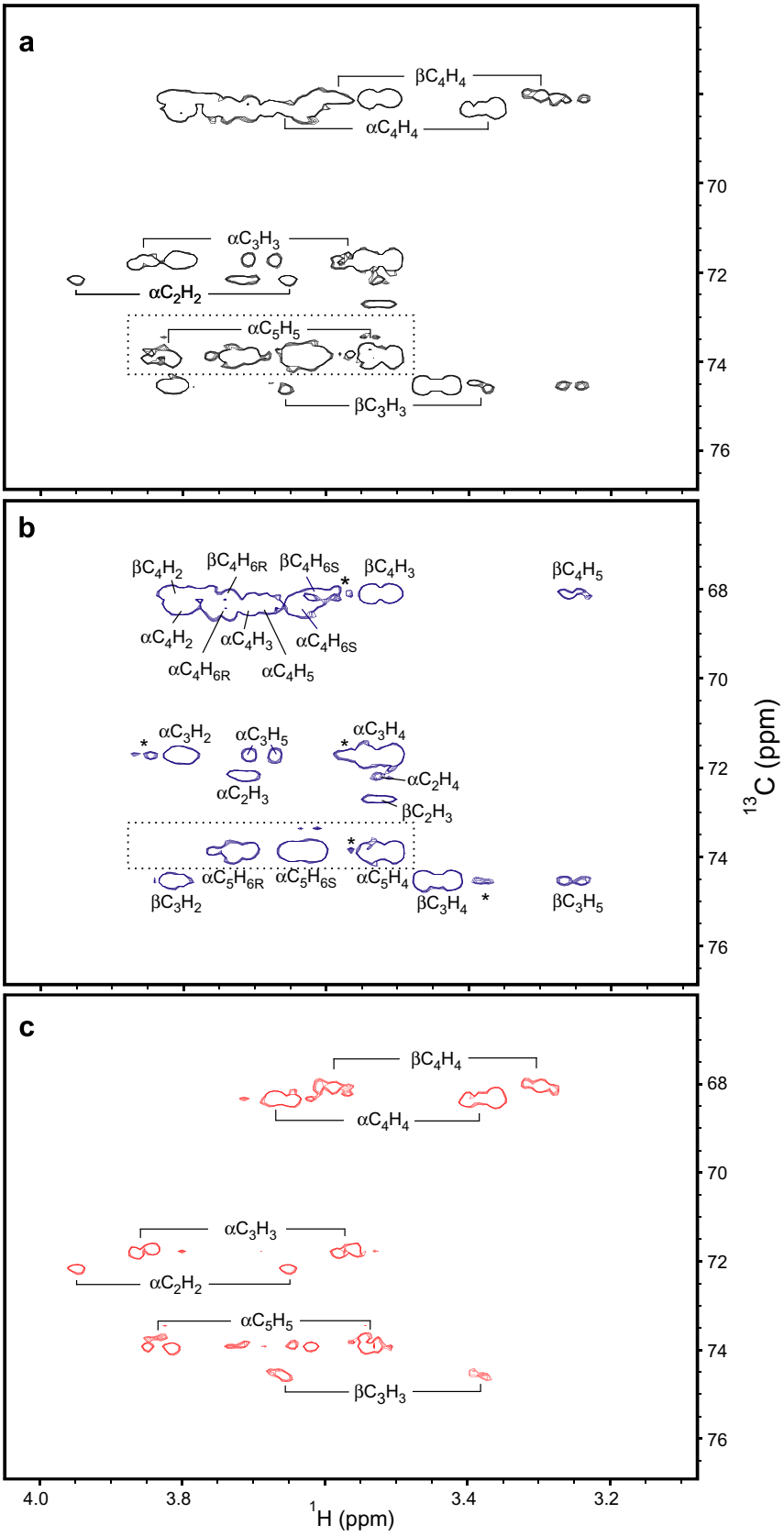

Fig. 6. Expansion of the bulk region framed in Fig. 5. (a) Conventional HMBC spectrum with strong-coupling induced one-bond correlations indicated. (b) *Clean* HMBC with long-range correlations indicated. Incompletely suppressed strong-coupling artifacts are marked by asterisks. (c) Illustration of one-bond signals suppressed by *clean* HMBC: the data sets are obtained by an HMBC experiment with a 3rd order initial LPJF and a 2nd order terminal high-pass *J* filter and otherwise recorded and processed as given in the caption to Fig. 5.

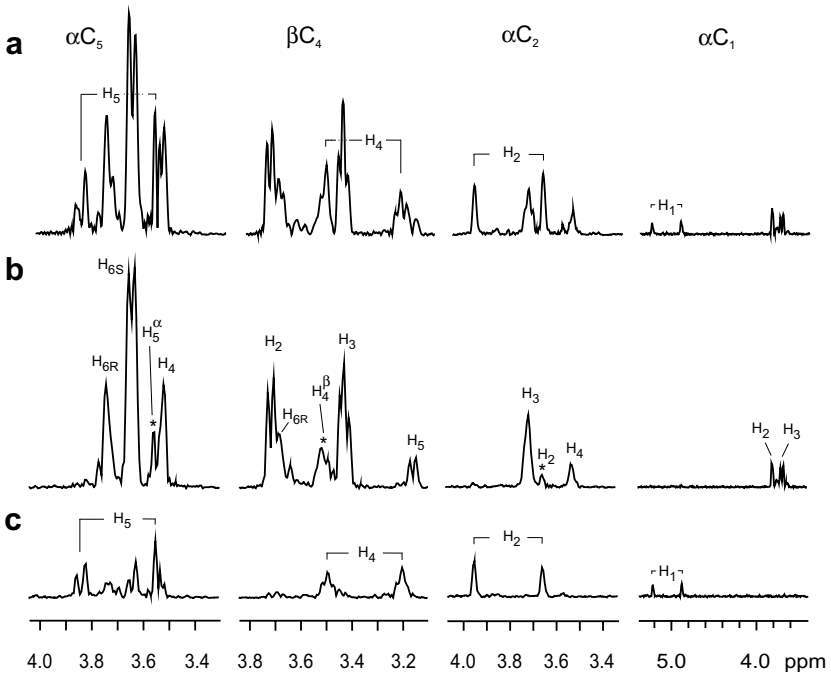

Fig. 7. 1D sections from (a) conventional HMBC spectrum, (b) *clean* HMBC spectrum, and (c) the spectrum from the special HMBC experiment with an initial LPJF and a terminal high-pass J filter to select strong-coupling induced artifacts (same data set as in Fig. 6c). The sections are taken along the F_2 axes at the ^{13}C frequencies of the indicated nuclei. Incompletely suppressed strong-coupling induced signals are indicated by asterisks in the *clean* HMBC sections in (b).

7. Experimental demonstration of clean HMBC

The experimental performance of the *clean* HMBC experiment is compared to that of conventional HMBC for the case of mannose in Fig. 5. The HMBC spectrum with an initial 3rd order LPJF (Fig. 5a) exhibits several one-bond correlations. In the *clean* HMBC spectrum (Fig. 5b) recorded with an overall 3rd order LPJF according to Fig. 1c these undesired artifacts are largely suppressed due to the novel positioning of the LPJF. In particular the bulk region of the spectrum, expanded in Fig. 6, contains several strongly coupled spin systems. Consequently, a number of one-bond correlations with $^1J_{CH}$ splittings are visible despite application of an initial 3rd order LPJF. These signals persist when the initial LPJF is extended to 4th order, but are suppressed by the proposed *clean* HMBC filtering scheme. Fig. 6a depicts the conventional HMBC spectrum with one-bond correlations indicated. All but two possible one-bond correlations in the bulk region show up with considerable intensity. In contrast, in the *clean* HMBC spectrum (Fig. 6b) the vast majority of one-bond correlations are absent.

In order to get a clear picture of the artifacts suppressed in *clean* HMBC, an experiment was performed with an initial 3rd order LPJF combined with the two-step *J* filter at the end in the high-pass version [4] to suppress the long-range and retain only one-bond correlations. The result is shown in Fig. 6c and these artifacts can be found with comparable intensities in the conventional HMBC spectrum of Fig. 6a but to a much smaller degree in the *clean* HMBC spectrum in Fig. 6b.

The simulated spectra of the $\alpha H_5H_4C_5$ ABX subsystem of mannose in Fig. 4 and the experimental spectra in Fig. 6 are in good agreement. In general, the notable difference between the ABX simulations and the experimental mannose spectrum is the numerous homonuclear couplings blurring the signals in both dimensions. Along with the coarse resolution this renders the strong-coupling frequency shift of the most strongly coupled spin subset ($\Lambda_\alpha = 11$ Hz in the exemplified case) overlap with the signals at ω_X in the indirect dimension. The strong-coupling shift Λ_β of the other spin subset is normally not visible owing to its low intensity. However, in this case it is visible about 0.5 ppm upfield from the main one-bond correlation. In agreement with the *clean* HMBC simulation in Fig. 4c, a minor part of the $\alpha C_5H_5^\alpha$ signal persists, owing to the incomplete filtering by the terminal LPJF. The corresponding X^β part of the signal at the same F_1 frequency is suppressed completely by the filter.

The performance and importance of the strong-coupling artifact suppression filter is further illustrated in Fig. 7 where 1D sections from four different ^{13}C nuclei are shown for conventional HMBC and *clean* HMBC spectra. The first section example is again the simulated case taken at the frequency of αC_5. The one-bond correlation is suppressed except for its low-frequency part. For the β-C_4 section the filtering is vital for resolving the correlation with H_5. The section of αC_2 demonstrates that the intensity of strong-coupling induced one-bond signals can be larger than those of the long-range correlations. A tiny fraction of the $\alpha C_2H_2^\beta$ signal, $\sim$1/10 of the original intensity, is still visible though. Fig. 7c contains the corresponding 1D sections taken out of the data shown in Fig. 6c.

8. Conclusion

In conclusion, we have introduced a new pulse sequence, *clean* HMBC that features effective suppression of strong-coupling induced artifacts in HMBC-type experiments. The novel filtering is achieved without sensitivity loss. In addition, it was shown that H2BC is rather insensitive to artifacts of strong coupling origin. The *clean* HMBC pulse sequence seems to be the HMBC sequence of choice in systems notorious for strong coupling, such as e.g., carbohydrates and oligosaccharides. Finally, the novel low-pass *J* filtering scheme can equally well be applied for suppression of strong-coupling induced artifacts in other variants of HMBC such as e.g., HAT HMBC [11] and edited HMBC [12].

Acknowledgments

P.W. is supported by a fellowship from Finnish National Graduate School in Informational and Structural Biology. This work was

financially supported by the Grant 122170 from the Academy of Finland to P.P. N.C.N. acknowledges support from the Danish National Research Foundation and the Danish Natural Science Research Council.

References

[1] A. Bax, M. Summers, ^{1}H and ^{13}C assignments from sensitivity-enhanced detection of heteronuclear multiple-bond connectivity by 2D multiple quantum NMR, J. Am. Chem. Soc. 108 (1986) 2093–2094.
[2] N.T. Nyberg, J.Ø. Duus, O.W. Sørensen, Heteronuclear two-bond correlation: suppressing heteronuclear three-bond or higher NMR correlations while enhancing two-bond correlations even for vanishing $^{2}J_{CH}$, J. Am. Chem. Soc. 127 (2005) 6154–6155.
[3] B.O. Petersen, E. Vinogradov, W. Kay, P. Würtz, N.T. Nyberg, J.Ø. Duus, O.W. Sørensen, H2BC: a new technique for NMR analysis of complex carbohydrates, Carbohydr. Res. 341 (2006) 550–556.
[4] A. Meissner, O.W. Sørensen, Economizing spectrometer time and broadband excitation in small-molecule heteronuclear NMR correlation spectroscopy. Broadband HMBC, Magn. Reson. Chem. 38 (2000) 981–984.
[5] T. Schulte-Herbrüggen, A. Meissner, A. Papanikos, M. Meldal, O.W. Sørensen, Optimizing delays in the MBOB, broadband HMBC, and broadband XLOC NMR pulse sequences, J. Magn. Reson. 156 (2002) 282–294.
[6] H. Kogler, O.W. Sørensen, G. Bodenhausen, R.R. Ernst, Low-pass *J* filters. Suppression of neighbor peaks in heteronuclear relayed correlation spectra, J. Magn. Reson. 55 (1983) 157–163.
[7] M.J. Thrippleton, R.A. Edden, J.J. Keeler, Suppression of strong coupling artefacts in *J*-spectra, Magn. Reson. 174 (2005) 97–109.
[8] J.A. Pople, W.G. Schneider, H.J. Bernstein, High-resolution Nuclear Magnetic Resonance, McGraw-Hill, New York, 1959.
[9] R.R. Ernst, G. Bodenhausen, A. Wokaun, Principles of Nuclear Magnetic Resonance in One and Two Dimensions, Clarendon Press, Oxford, 1987.
[10] A. Kumar, Two-dimensional spin-echo NMR spectroscopy: a general method for calculation of spectra, J. Magn. Reson. 30 (1978) 227–249.
[11] A.J. Benie, O.W. Sørensen, HAT HMBC: a hybrid of H2BC and HMBC overcoming shortcomings of both, J. Magn. Reson. 184 (2007) 315–321.
[12] A.J. Benie, O.W. Sørensen, Improved multiplicity-editing of HMBC NMR spectra, Magn. Reson. Chem. 44 (2006) 739–743.
[13] M. Bak, J.T. Rasmussen, N.C. Nielsen, SIMPSON: a general simulation program for solid-state NMR spectroscopy, J. Magn. Reson. 147 (2000) 296–330.
[14] F. Delagio, S. Greziek, G. Vuister, G. Zhu, J. Pfeifer, A. Bax, NMRPipe: a multidimensional spectral processing system based on UNIX pipes, J. Biomol. NMR 6 (1995) 277–293.